Binding of electrons, holes, and excitons in symmetric strained $InP/In_{0.49}Ga_{0.51}P$ triple quantum-dot molecules

M. Tadić* and F. M. Peeters†

Departement Natuurkunde, Universiteit Antwerpen (Campus Drie Eiken), Universiteitsplein 1, B-2610 Antwerpen, Belgium

(Received 26 September 2003; revised manuscript received 24 May 2004; published 3 November 2004)

The electron, hole, and exciton spectra in the strained quantum-dot molecule consisting of three vertically arranged type-II $InP/In_{0.49}Ga_{0.51}P$ self-assembled quantum dots are modeled by the $\mathbf{k}\cdot\mathbf{p}$ theory. For the sake of simplicity, we consider dots of cylindrical shape, but take into account the anisotropy of the strain through the continuum mechanical model. For thick spacers, the strain leads to an upward shift of the lowest energies in all explored electron shells, but for spacers thinner than, say, the *coupling length*, the quantum mechanical coupling prevails, and downward shifts are observed. The magnitudes of both the energy shift and the coupling length vary with the quantum-dot height. For the holes, the interplay of strain and mixing enables binding at larger distances than for the electrons. The overlap of the hole clouds is basically established by means of the light holes, which are confined by the strain in the spacer between the dots and may efficiently couple the heavy-hole states, which are localized inside the quantum dots. Similar to electrons, the exciton lowest-energy states of different angular momenta, as computed by an exact-diagonalization approach, exhibit overshoots on the single-quantum-dot levels. Good agreement is found with experiment on the spatial location of electrons and holes in the triple-quantum-dot molecules.

DOI: 10.1103/PhysRevB.70.195302 PACS number(s): 73.21.La, 78.67.Hc, 71.35.−y, 71.35.Cc

I. INTRODUCTION

A great deal of interest has been recently devoted towards exploring quantum dots, where the electrons are confined in all three spatial directions, like in atoms.[1,2] Various techniques have been used to produce tiny islands of quantum dots, but the Stranski-Krastanow growth mode, which enables quantum dots to self-assemble, seems to be the most promising contender for technologies of the future, as lasers,[3] optical amplifiers,[4] photonic detectors,[5] resonant tunneling devices,[6] or memory elements.[7] Moreover, it was demonstrated that the strain fields promote growth of one self-assembled quantum dot (SAQD) directly above another,[8,9] resulting in stacked quantum dots. The states of individual dots in these stacks bind in a molecular manner, as demonstrated by the splitting of the single-quantum-dot (SQD) levels into multiplets composed of bonding and antibonding states. In quantum-dot molecules made of etched quantum dots, a parabolic confinement potential, for which the shell structure is described by Hund-like rules,[10,11] is usually assumed when computing the electronic structure. It turns out, however, that for SAQD's, where nonuniform strain, which arises from the lattice mismatch between the dot and the matrix, is inherently present, such simple parabolic model potentials are of limited validity.

By using the single-band model applied to the conduction band, Fonseca *et al.*[12] explored the influence of strain and piezoelectric fields on the energy levels in pyramidal InAs/GaAs quantum dots. The splitting of the energy levels was demonstrated in quantum-wire structures formed by periodically repeating InAs/GaAs quantum dots in the vertical direction.[13] Recently, Schliwa *et al.*[14] performed calculations of the hole and exciton levels in InAs/GaAs double-dot molecules by means of the 8×8 multiband $\mathbf{k}\cdot\mathbf{p}$ theory. Antibonding behavior of the ground hole levels for spacers thinner than about 5 nm was found. More recently, the 8×8 $\mathbf{k}\cdot\mathbf{p}$ model was employed to calculate the electronic structure in stacks of truncated pyramidal InAs/GaAs quantum dots in an external electric field.[15] In InP/InGaP SAQD's, which attracted less attention, a heuristic model was proposed which claims to be able to qualitatively account for magnetophotoluminescence measurements.[16] According to this model, the electrons are localized inside the dots, while the holes are located in the spacers. Recent experiments performed on larger InP/InGaP quantum dots than in Ref. 16 indicate that the multiparticle states are considerably affected by the size of the dot,[17] which should also occur in quantum-dot molecules when the spacer thickness varies.

In this paper, we go beyond the heuristic predictions of Ref. 16, with the aim of providing a consistent explanation of the spatial localization of electrons, holes, and excitons in stacks composed of disk-shaped quantum dots. We will consider quantum-dot molecules consisting of three cylindrical InP quantum dots embedded into the $In_{0.49}Ga_{0.51}P$ matrix. For the case of a thin single InP/InGaP quantum dot, we recently found that the z projection of the total angular momentum of the ground hole level amounts to $3\hbar/2$, while considerable localization of the light holes outside the dot near the interface between the dot and matrix switches the z projection of the total angular momentum in the ground state to $\hbar/2$ as the height of the dot increases.[18] Without strain, the InP/InGaP quantum dot is a type-II structure, but the strain reverts the band alignment to type I. Because of the small value of the valence band offset, experimental verification of the type of the band alignment is not an easy task, but as confirmed by recent single-band calculations for InP/InGaP SAQD's, the exciton energy levels are not considerably affected by the assumed type of the band alignment.[19] In our approach the strain distribution is extracted from the continuum mechanical (CM) model, which was solved numeri-

cally using the finite-element method. InP and InGaP are large-band-gap semiconductors, which allows us to consider the conduction band (CB) and the valence bands (VB's) separately. Both the electron and hole Hamiltonians are simplified to axially symmetric forms. We follow the electron, hole, and exciton states in symmetric stacks of three strained dots as they evolve from the respective SQD states. In order to calculate the exciton states, an exact-diagonalization approach, able to properly take into account both the coupling and symmetry, is employed. Finally, we compare the theory for symmetrical quantum dot stacks with the experimental results of Ref. 16.

The aim of the present paper is to indicate trends of how, e.g., the exciton energies vary with the interdot distance in vertically coupled quantum dots. For example, we found that the quantum-dot molecule undergoes a type-I to type-II transition as a function of the interdot distance (d). Furthermore, an interesting interplay between the heavy holes and light holes is found as function of d and the hole interdot coupling is mainly mediated by the light holes. In the present paper, we restrict ourselves to disk-shaped quantum dots because of the following reasons: (1) they are the most simple realistic model with the minimum number of parameters, (2) currently no detailed knowledge of the shape and alloy composition of the InP/InGaP single and stacked quantum dots is known, and (3) experiments on an ensemble of quantum dots average out the finer details resulting from the exact shape of the quantum dots.

The paper is organized as follows. In Sec. II the models used to calculate the strain fields and the single-particle electronic structure are briefly outlined. The theoretical frameworks for the exciton states and the oscillator strength are detailed. The results of our calculation for stacks of three InP/InGaP SAQD's are discussed in Sec. III. Our conclusions are summarized in Sec. IV.

II. MODEL

A. Strain and single-particle electronic structure

The low-lying states of electrons, holes, and excitons are our main objective; therefore, the thin wetting layers, which are responsible for the leakage of the zero-dimensional (0D) states into the two-dimensional (2D) states near the energy continuum, may be discarded without substantial loss of accuracy. This approximation is found to be harmless for the low-lying states in InAs/GaAs quantum dots,[20,21] and we expect that this also holds for the present InP/InGaP quantum dots. By neglecting the wetting layers and adopting equal distances between the dots, the stacks of three quantum dots of equal size become symmetric with respect to the $z=0$ plane.

A sketch of a triple-dot molecule (TDM) composed of SAQD's (shaded areas) separated by d with respect to each other is displayed in Fig. 1(a), and the grids along the z and ρ directions used to compute the strain are shown in Figs. 1(b) and 1(c), respectively. The grid points depend on the counter i, and they are adopted for the quantum-dot height of $h=3$ nm, radius of $R=8$ nm, and spacing between the dots of $d=6$ nm. The molecules are placed inside a large cylinder of

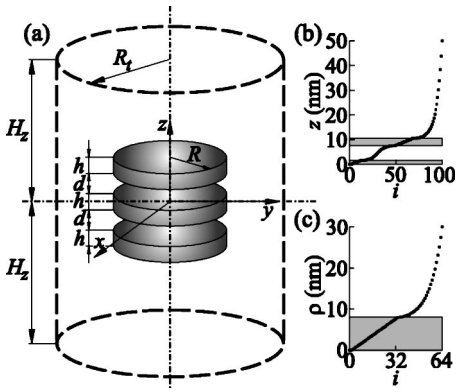

FIG. 1. (a) Sketch of a triple-dot molecule (TDM) composed of stacked InP dots (indicated by the shaded areas) of radius R and height h, symmetrically arranged with respect to the $z=0$ plane and separated by the InGaP spacer of thickness d. The simulation area is given by the large cylinder. The distribution of the grid points used in the strain calculation for $h=3$ nm, $R=8$ nm, and $d=6$ nm along the z direction (b) and along the ρ direction (c).

radius R_t and height $2H_z$ which is employed to discretize the displacements by the first-order finite elements onto a nonuniform grid and to subsequently expand the single-particle wave functions.[18] The Cartesian coordinates x, y, and z in Fig. 1 coincide with the [100], [010], and [001] crystallographic directions, respectively. Furthermore, relying on the symmetry of the molecule, the strain calculation can be alleviated by restricting ourselves to the first octant only.[18] Rigid boundary conditions are imposed for the displacements at the boundary of the domain ($\rho=R_t, z=H_z$).

The wave functions of electrons, holes, and excitons are expanded on the cylinder $\rho \leqslant R_t$, $|z| \leqslant H_z$. Referring to the large band gaps of the constituent materials, the CB electrons are considered uncoupled from the VB ones, while the mixing between the heavy-hole (hh), light-hole (lh) and the split-off (so) bands is explicitly taken into account through the 6×6 Pikus-Bir $\mathbf{k}\cdot\mathbf{p}$ Hamiltonian.[18] In cylindrical quantum dots, the confining potentials due to the band offsets exhibit full axial symmetry, which is, however, not the case for all components of the strain tensor, where a considerable in-plane anisotropy is found. However, the linear combinations of the strain tensor components which detrimentally affect the electronic structure exhibit negligible in-plane anisotropy, which allows us to recast the original CB and VB Hamiltonians into axially symmetric forms. The axial symmetry of the Hamiltonian is additionally imposed by neglecting both the bulk in-plane warping of all VB's and the shear strains and averaging the diagonal components of the strain tensor over the azimuthal angle. The states of the electrons in the conduction and the valence bands are classified according to the z projection of the total angular momentum $F_z=f\hbar$, which is composed of the Bloch zone-center part $J_z=j\hbar$ and the envelope (orbital) part $L_z=l\hbar$. Here F_z, J_z, and L_z and the associated quantum numbers are additionally subscripted by e and h for electrons and holes, respectively. For the valence band, the states of different L_{zh} are mixed by the Hamiltonian, while l_e and the electron spin $j_e=s$ are separately good quantum numbers for the electrons. Furthermore,

the symmetry of the system allows the classification of all states according to their parity. The VB spinors for the even and odd states have the forms

$$F_{f_h}^{(+)} = \begin{bmatrix} F_{hh,l_{h1}}^{(+)} \\ F_{lh,l_{h2}}^{(-)} \\ F_{so,l_{h3}}^{(-)} \\ F_{hh,l_{h4}}^{(-)} \\ F_{lh,l_{h5}}^{(+)} \\ F_{so,l_{h6}}^{(+)} \end{bmatrix}, \quad F_{f_h}^{(-)} = \begin{bmatrix} F_{hh,l_{h1}}^{(-)} \\ F_{lh,l_{h2}}^{(+)} \\ F_{so,l_{h3}}^{(+)} \\ F_{hh,l_{h4}}^{(+)} \\ F_{lh,l_{h5}}^{(-)} \\ F_{so,l_{h6}}^{(-)} \end{bmatrix}, \tag{1}$$

respectively. Here F_{hh}, F_{lh}, and F_{so} denote hh, lh, and so envelope functions, the parity is indicated in the superscript, and l_{hj} $(j=1,2,\ldots,6)$ denotes the orbital momentum of the VB electron for the given F_{zh}. We further refer to the VB states as hole states, keeping in mind that the Hamiltonian is written for the electrons in the valence band and appropriately taking into account the phases of these envelope functions when calculating exciton states.[22]

Following Refs. 18 and 23, the eigenstates of the holes are labeled by $nX_{f_h}^{\sigma}$, where σ denotes the state's parity, n is the principal quantum number for the given f_h and σ, and X denotes the lowest $|l_h|$ among the six envelope functions of the holes. As an example, the set of envelope functions which corresponds to the $S_{3/2}^{+}$ shell is

$$F_{3/2}^{(+)} = [F_{hh,0}^{(+)}, F_{lh,1}^{(-)}, F_{so,1}^{(-)}, F_{hh,3}^{(-)}, F_{lh,2}^{(+)}, F_{so,2}^{(+)}]^T. \tag{2}$$

Therefore, $l_{h1}=0$, and the lowest kinetic energy belongs to the heavy holes. In the other example of the $S_{1/2}^{-}$ shell,

$$F_{1/2}^{(-)} = [F_{hh,-1}^{(-)}, F_{lh,0}^{(+)}, F_{so,0}^{(+)}, F_{hh,2}^{(+)}, F_{lh,1}^{(-)}, F_{so,1}^{(-)}]^T, \tag{3}$$

the l_{h2} of the light holes equals zero. We point out here that the $X_{f_h}^{\pm}$ states are Kramers degenerate with the $X_{-f_h}^{\mp}$ states, and therefore they have equally distributed probability density (PD), computed as $(F_{f_h}^{\sigma})^{\dagger}F_{f_h}^{\sigma}$. Because of the spin degeneracy, no notion in the symbol for the electron states, l_e^{σ}, is given to the total angular momentum (or equivalently the spin) of the electron.

The dependence of envelope functions on the polar angle is given explicitly in our axially symmetric approach. As a consequence, Hamiltonian matrices of order only a few thousand have to be diagonalized, which are considerably smaller than in a full 3D calculation, where one is forced to handle matrices of order a few million. We indeed found that the subtle details related to the piezoelectricity and the shear strains missing in the axially symmetric model improve the results for the electron and hole energies by less than a meV, as also found by Fonseca *et al.*[12] for larger pyramidal quantum dots. Moreover, the axially symmetric model enables a simple analysis of the binding of electrons and holes in terms of strain-mediated effective potentials and orbital momenta of different Bloch states. With other words, the removal of axial symmetry due to anisotropy of the strain fields in the cylindrical quantum dots effectively couples states of different orbital momenta of electrons and holes, which makes the physical interpretation of the results less transparent.

B. Exciton states

The exciton eigenvalues E_{exc} and eigenfunctions Ψ_{exc} are extracted from the Schrödinger equation

$$(H_e - H_h + V_C)\Psi_{exc} = E_{exc}\Psi_{exc}. \tag{4}$$

Here H_e and H_h are the electron and hole Hamiltonians, respectively, and V_C is the Coulomb potential energy,

$$V_C = -\frac{q^2}{4\pi\epsilon\epsilon_0}\frac{1}{|\mathbf{r}_e - \mathbf{r}_h|}, \tag{5}$$

where $\mathbf{r}_e$ and $\mathbf{r}_h$ denote the electron and hole position, respectively, and the relative permittivity ϵ is taken to be equal in the two semiconductors. The exciton wave function is expanded into pairs formed by the zone-center single-particle electron and hole wave functions,

$$\Psi_{exc}(\mathbf{r}_e, \mathbf{r}_h) = \sum_{s,j_h} F_{s,j_h}(\mathbf{r}_e, \mathbf{r}_h)|s\rangle|j_h\rangle, \tag{6}$$

where s denotes the electron spin ($\uparrow$ or $\downarrow$), j_h is the magnetic quantum number of holes and F_{s,j_h} the envelope function of the exciton. Since the Coulomb potential energy depends on neither the electron spin nor the hole magnetic quantum number, it cannot couple states of different s and j_h. Furthermore, the whole exciton may be rotated by 2π about the z axis without modifying its internal structure, which implies that the z component of the angular momentum, $F_{zexc}=F_{ze}-F_{zh}$, is a good quantum number for the excitons. The exciton envelope functions are arranged into spinors, which are for the given electron spin s expanded into pairs of electron and hole envelope functions,

$$F_{exc,s}(\mathbf{r}_e, \mathbf{r}_h) = \begin{bmatrix} F_{s,1} \\ F_{s,2} \\ F_{s,3} \\ F_{s,4} \\ F_{s,5} \\ F_{s,6} \end{bmatrix} = \sum_m \sum_n a_{mn} \begin{bmatrix} F_{hm1} \\ F_{hm2} \\ F_{hm3} \\ F_{hm4} \\ F_{hm5} \\ F_{hm6} \end{bmatrix} F_{en,s}, \tag{7}$$

with the appropriate phases for the holes.[22] Here F_{hmi} denotes the ith envelope function of the mth hole state in the reduced notation with respect to the one given in Eq. (1), n is the number of the CB electron state for the given electron spin s, and a_{mn} are the expansion coefficients. The electron and hole labels n and m run over the z projections of the angular momenta l_e and F_{zh} which satisfy

$$F_{zexc} = (s + l_e)\hbar - F_{zh}, \tag{8}$$

for the given electron spin s indicated in the subscript of the electron envelope function [see Eq. (7)]. The expansion in Eq. (6) yields the secular equation

$$(E_{en} - E_{hm} - E_{exc})\,\delta_{im}\delta_{kn} + \sum_{m}\sum_{n}\sum_{j=1}^{6}\langle F_{hij}F_{ek}|V_C|F_{hmj}F_{en}\rangle = 0, \tag{9}$$

where E_{en} and E_{hm} denote the single-particle electron and hole energies and δ is the Kronecker symbol. The six-dimensional Coulomb matrix element

$$\langle F_{hij}F_{ek}|V_C|F_{hmj}F_{en}\rangle = \int_{\Omega} O_e(\mathbf{r}_e)O_h(\mathbf{r}_h)V_C(\mathbf{r}_e - \mathbf{r}_h)d\mathbf{r}_e d\mathbf{r}_h, \tag{10}$$

contains overlap (product) functions between different states of holes and electrons, $O_h = F^*_{hij}F_{hmj}$ and $O_e = F^*_{ek}F_{en}$, respectively. Using Fourier transform and Parseval's identity, the six-dimensional integral in Eq. (10) may be simplified to the three-dimensional integral in Fourier space,

$$\langle F_{hij}F_{ek}|V_C|F_{hmj}F_{en}\rangle = \frac{1}{2\pi^3}\int_{\Omega_{\mathbf{k}}} \mathcal{F}_e(-\mathbf{k})\mathcal{F}_h(\mathbf{k})\mathcal{V}_C(\mathbf{k})d\mathbf{k}, \tag{11}$$

where $V_C = 1/(\epsilon\epsilon_0|k|^2)$ is the Fourier transform of V_C, while the Fourier transforms of the electron and hole overlap functions, $\mathcal{F}_e$ and $\mathcal{F}_h$, read

$$\mathcal{F} = i^{|l_i - l_k|}e^{i(l_i - l_k)\varphi_{\mathbf{k}}} \times \int_0^{\infty}\rho d\rho \int_{-\infty}^{+\infty} dz D(\rho,z)J_{|l_i - l_k|}(k_t\rho)e^{ik_z z}. \tag{12}$$

Here $D(\rho,z)$ denotes the part of the overlap function which depends only on ρ and z, $J_{|l_i - l_k|}$ is the Bessel function of order $|l_i - l_k|$, l_i and l_k are the orbital quantum numbers of the envelope functions involved in the overlaps, and $\varphi_{\mathbf{k}}$, k_t, and k_z are the cylindrical coordinates of the wave vector in Fourier space. Hence, the Fourier transforms of the overlap functions reduce to the complex Fourier transform along z and the Hankel transform of order $|l_i - l_k|$ along the ρ direction.

The four types of electron and hole overlap functions may be classified according to the parity of the states involved in the overlaps: $F^{(+)}_{hij}F^{(+)}_{ek}$, $F^{(+)}_{hij}F^{(-)}_{ek}$, $F^{(-)}_{hij}F^{(+)}_{ek}$, and $F^{(-)}_{hij}F^{(-)}_{ek}$. The specific form of the integral in Eq. (11) classifies the pairs of electron and hole wave functions into two distinct groups, one containing pairs of wave functions of the same parity, $F^{(+)}_{hij}F^{(+)}_{ek}$, $F^{(-)}_{hij}F^{(-)}_{ek}$, which contributes to say, the even exciton states ($\sigma_{exc} = +$), whereas the states of the opposite parity, $F^{(+)}_{hij}F^{(-)}_{ek}$, $F^{(-)}_{hij}F^{(+)}_{ek}$, take part in the odd-parity excitons ($\sigma_{exc} = -$). Moreover, the $\mathbf{k}$ integral in Eq. (11) can be reduced to

$$\langle F_{hij}F_{ek}|V_C|F_{hmj}F_{en}\rangle = \frac{2}{\pi}\delta_{l_{ek}-l_{hij},l_{en}-l_{hmj}}\int_0^{\infty} dk_t k_t \int_0^{\infty} dk_z \frac{\mathcal{G}(k_t,k_z)}{k_t^2 + k_z^2}, \tag{13}$$

where $\mathcal{G}$ denotes the product of the Fourier transforms of the electron and hole pair functions,

$$\mathcal{G}(k_t,k_z) = \begin{cases} \mathrm{Re}(\mathcal{F}_h)\mathrm{Re}(\mathcal{F}_e), & \sigma_{exc} = +, \\ \mathrm{Im}(\mathcal{F}_h)\mathrm{Im}(\mathcal{F}_e), & \sigma_{exc} = -. \end{cases} \tag{14}$$

Without the magnetic field, there is a degeneracy with respect to the *electron spin*, but the z projection of the total angular momentum of the exciton depends on the electron spin; therefore, the exciton states are denoted as $nX^{\sigma_{exc}}_{f_{exc\uparrow}}$ and $nX^{\sigma_{exc}}_{f_{exc\downarrow}}$ for electron spin up and spin down, respectively, and $F_{zexc} = f_{exc}\hbar$, while the other symbols have the same meaning as for the holes, as explained in Sec. II A.

The electron and hole of an exciton recombine in a single point; therefore, the relevant space for the oscillator strength is defined by $\mathbf{r}_e = \mathbf{r}_h = \mathbf{r}$, which led us to compute

$$|F_{exc,s}|^2_{2D} = \frac{1}{2\pi}\int_0^{2\pi} F^{\dagger}_{exc,s}(\mathbf{r},\mathbf{r})F_{exc,s}(\mathbf{r},\mathbf{r})d\varphi, \tag{15}$$

as a reasonable assessment of the spatial localization of an exciton. Further, we will refer to this quantity as the 2D exciton probability density (2DPD). In order to assess the contributions of different valence bands to the exciton states,

$$p_{vb,exc} = \int_{\Omega} (|F_{s,i}(\mathbf{r},\mathbf{r})|^2 + |F_{s,j}(\mathbf{r},\mathbf{r})|^2)d\Omega \tag{16}$$

is computed for $vb = \mathrm{hh}, \mathrm{lh}$, and so. Here, $F_{s,i}$ and $F_{s,j}$ denote the two envelope functions belonging to the designated band. Integration in Eq. (16) is performed over the domain ($\rho \leqslant R_t$, $|z| \leqslant H_z$), shown in Fig. 1.

III. RESULTS AND DISCUSSION

The numerical work was done for InP/InGaP quantum-dot molecule, which consists of three identical quantum dots of radius $R = 8$ nm. For the height, we choose three different values $h = 2$, 3, and 4 nm, while the thickness of the InGaP spacer in TDM's varied from $d = 0$ to 20 nm by steps of 0.25 nm. The material parameters are listed in Table I of Ref. 18. The VB offset taken in our calculation amounts to −45 meV, as employed in the multiband $\mathbf{k}\cdot\mathbf{p}$ calculations for truncated pyramidal SQD's.[24] The domain displayed as the large cylinder in Fig. 1 for the TDM has a radius of $R_t = 30$ nm and height $2H_z = 100$ nm. For the strain calculation the grid contains 33 vertices along φ, 65 vertices along ρ, and 101 vertices along the z direction. The nonuniform grid (see Fig. 1) is required to describe properly the abrupt variations of the elastic constants at the dot-matrix interface, where, e.g., the length of the finite elements adjacent to the interface was taken as low as 0.01 nm. In order to find the displacements at the grid points, we solve the system of about 6×10^5 linear equations by the conjugate gradient algorithm.

The electron and hole wave functions are expanded into a basis consisting of products of 10 ρ-dependent Bessel functions of the appropriate order and 100 sin/cos functions along z. Only half of the z-dependent functions are employed for each parity of the electron states, and the calculation of the hole states was similarly simplified.[18] The Hamiltonian

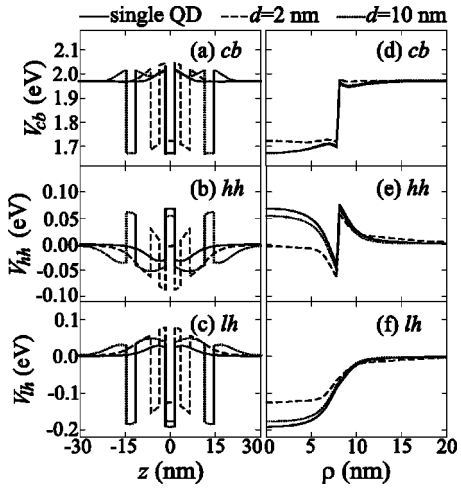

FIG. 2. The angular averaged effective potentials in the triple-dot molecule (TDM) composed of 3-nm-high quantum dots, along the z and ρ axes, are shown for $d=2$ nm (dashed lines) and $d=10$ nm (dotted lines). The SQD case (solid line) is added for comparison. The left panel shows variations of the effective potentials along the z axis: (a) the CB, (b) the hh band, and (c) the lh band. The right panel shows the effective potentials along the ρ axis: (d) the CB, (e) the hh band, and (f) the lh band.

matrix for the exciton states was constructed out of a total of 320 pairs of electron and hole wave functions of the states closest to the band extrema in a restricted range of angular momenta, which for the electrons was $-2<l_e<2$ and for the holes $-9/2<f_h<9/2$. The exciton states are computed for both electron spins and five values of f_{exc} in the range $-2<f_{exc}<2$, where only some of the exciton states are found to be optically active. The electron and hole states in the quantum-dot molecules are classified as bonding and antibonding with regard to the position of the SQD energy level they originated from. For a bonding conduction (valence) band state in the quantum-dot molecule the energy level is below (above) the level in the SQD, and vice versa for an antibonding state.

A. Strain and effective potentials

The influence of the strain on the TDM consisting of cylindrical 3-nm-high InP/InGaP quantum dots is illustrated in Fig. 2, where the left panel [Figs. 2(a)–2(c)] shows effective potentials along $(\rho=0,z)$, while the right panel [Figs. 2(d)–2(f)] shows the angular averages of the effective potentials along the ρ direction. Along the z direction, the effective potentials in each of the three bands coincide with the respective band extrema.[25] In Fig. 2 the effective potentials in the SQD are compared with those in the TDM's containing $d=10$ and 2 nm thick spacers. Even for the spacer as thick as $d=10$ nm, the strain fields around the three dots interact, but they do not appreciably affect the bottom of the CB within the dots, which appears almost flat in Fig. 2(a). In other words, hydrostatic strains within the individual quantum dots are screened from each other. However, when the distance between the dots decreases to $d=2$ nm, the strain lifts and modifies the shape of the effective potential inside the satellite dots to a triangular form, pushes the effective potential inside the central dot towards even higher energies, and it considerably increases the bottom of the CB in the spacer. Due to the peculiar distribution of the hydrostatic strain, the CB bottom tends to the bulk value in the InGaP matrix from below. By reversing the energy axis, one may notice that the confinement of the heavy holes is modified by the strain in a similar way as for the CB electrons [see Fig. 2(b)]. But opposite to the electrons, the effect of the vicinity of the dots on the hh band is still present for $d=10$ nm, which is demonstrated by the nearly triangular shape of the satellite potential wells along the z direction and a rather large decrease of the confinement potential with respect to the SQD case. If the thickness of the spacer is reduced to 2 nm, the strain shallows further the effective potential wells inside the dots and increases the height of the barrier for the heavy holes in the spacer. For the spacers as thin as $d=2$ nm, the hh effective potential within the dots is strongly pushed down by the strain, while the triangular-shaped effective potential wells near the radial boundary remain. Therefore, the heavy holes may settle near the radial periphery when the spacer thickness decreases, as indeed was found by an earlier single band treatment.[26] Opposite to heavy holes, light holes are expelled by the strain to the matrix near the dot-matrix interface in the SQD, as shown in Fig. 2(c)—i.e., towards the top and bottom of the quantum dots. When d decreases, the strain creates an effective potential well for the light holes in the spacer and deepens the effective potential wells in the matrix. The barriers for the light holes formed in the dots are lowered and acquire a triangular shape when the spacing between the dots decreases. We also want to point out that the strain provides no confinement in the so band, but based on the strain-induced mixing between the lh and so bands, a non-negligible contribution of the so band to the hole states in the quantum dot is expected.

Figure 3 shows extrema of the effective potentials in the TDM along the z direction as they vary with the spacing between the dots. For small d, the maximum of the CB effective potential is located in the spacers, but this energy value decreases with d, eventually becoming lower than the value of the CB effective potential at the dot-barrier interface. As a consequence, a knee in the $V_{cb}^{max}(d)$ curve appears in the upper part of Fig. 3(a). For $h=3$ nm, the knee is located at $d=6.5$ nm. By further separating the quantum dots, the hydrostatic strain at the dot-matrix interface increases slightly, which in turn produces a slight increase of V_{cb}^{max} with d. For thin spacers, the rate of the decrease of V_{cb}^{min}, shown in the lower part of Fig. 3(a), is much larger, but for $d \gtrsim 10$ nm the V_{cb}^{min} becomes rather flat. Hence, we may consider 10 nm as the upper value of d for which screening due to strain is present in the TDM's. The maxima of the hh and lh effective potentials, shown in Figs. 3(b) and 3(c), cross, which makes the heavy holes more dominant for thick spacers and the light holes for thin spacers.

B. Electron and hole states

In addition to the vertical confinement, the electrons are confined laterally by the band offset and the strain (see Ref.

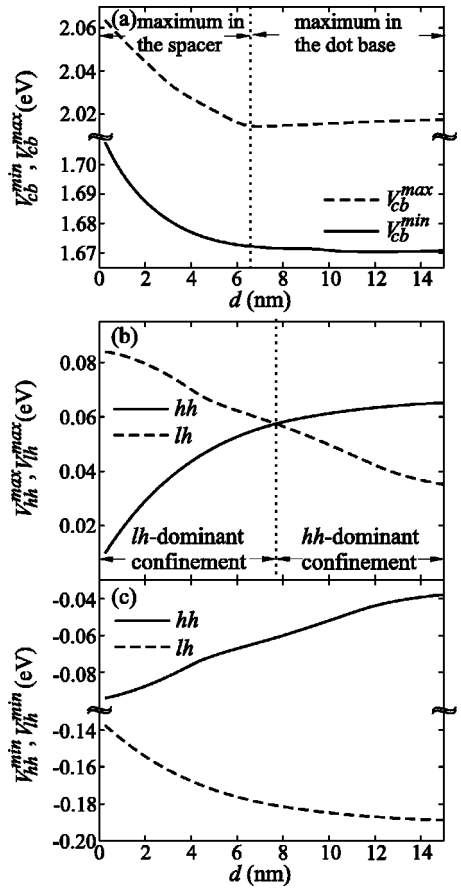

FIG. 3. Variations of the extrema of the effective potentials in the three bands along $(\rho=0,z)$ as function of the spacer thickness. The stack consists of 3-nm-high quantum dots. (a) The CB maximum is shown by the dashed line in the upper part, while the CB minimum is displayed by the solid line in the lower part. (b) The maxima of the hh (solid line) and lh (dashed line) effective potentials. (c) The minima of the hh (solid line) and lh (dashed line) effective potentials.

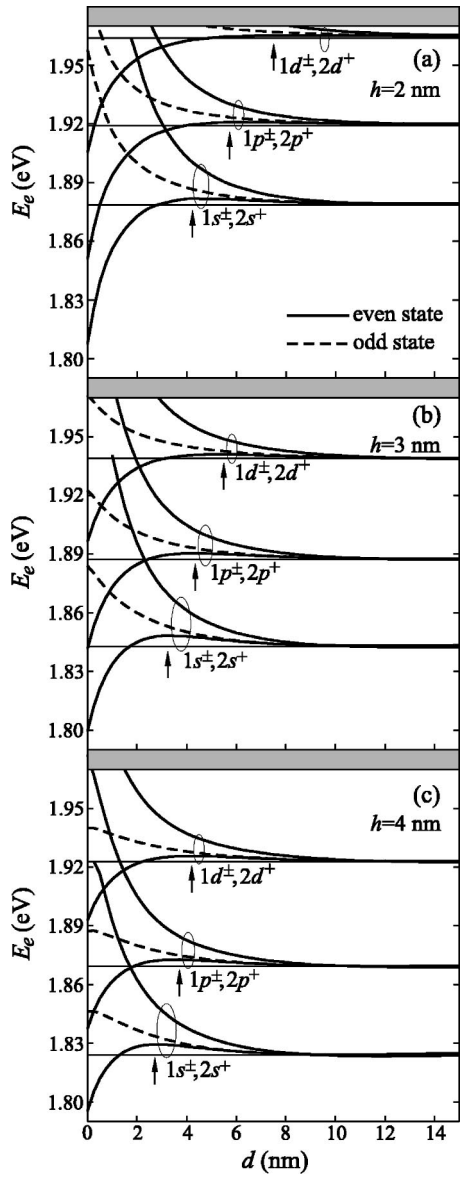

FIG. 4. The splitting of the CB energy levels in the TDM, for (a) $h=2$ nm, (b) $h=3$ nm, and (c) $h=4$ nm. The even- and odd-electron states are indicated by the solid and dashed lines, respectively. The values of the coupling length in different shells are indicated by the arrows. The shaded areas represent the energy continuum.

18 for the study on the confinement in single InP/InGaP quantum dots). In the axially symmetric model the electron energies depend on the orbital momentum, as shown in Figs. 4(a)–4(c) for $h=2$, 3, and 4 nm, respectively. The lowest-energy triplets in *s*, *p*, and *d* shells are displayed in Fig. 4 for each selected value of the quantum-dot height, and the convergence of the states in the triplets is demonstrated by adding thin horizontal lines, which represent the electron energies in the SQD. Note that the strain lifts the energies of the even states above the level in the SQD, which reverts bonding to antibonding behavior for thick spacers. The increase of the $1l_e^+$ energies indicate that the quantum mechanical coupling is ineffective for thick spacers, but opposes the strain, leading to a local maximum for a certain value of *d* and finally reverting the behavior to bonding-like for thin spacers. The distance $d=d_0$, where the overshoot is largest, indicates that the effect of strain on the electron energy is suppressed by the quantum mechanical coupling. For $d>d_0$ the electron energy levels are dominantly determined by strain, while for $d<d_0$ electron coupling between the two quantum dots produces the downward shifts; therefore, we consider d_0 as the distance at which quantum mechanical coupling becomes important and refer it to as the *coupling length*. In the strain-free systems, where the effective potentials due to band offsets are constrained to the dots, d_0 tends to infinity. The coupling length d_0 depends on (1) the electron orbital momentum, which diminishes the impact of strain by imparting more kinetic energy to the electrons, and (2) the height of the quantum dot, which alters the distribution of the strain field. A larger d_0 is found for larger l_e and thinner quantum dots.

According to the number of dots present in the system, one may anticipate splitting of the SQD hole levels into triplets. However, the hole levels, shown in Fig. 5, do not exhibit a simple triplet structure. Only for large *d* do the different levels converge to a triplet whose interlevel distance de-

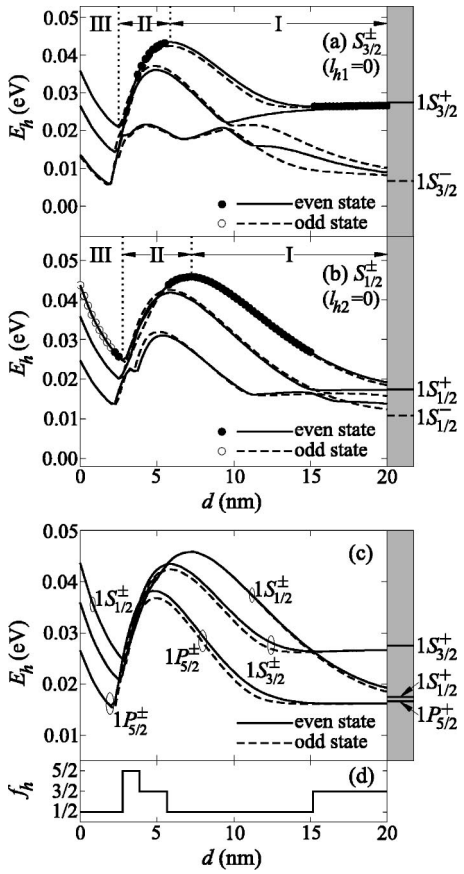

FIG. 5. The VB levels in TDM's as a function of the spacer thickness for (a) $S^{\pm}_{3/2}$ states, (b) $S^{\pm}_{1/2}$ states, and (c) the highest-energy VB states of $S^{\pm}_{3/2}$, $S^{\pm}_{1/2}$, and $P^{\pm}_{5/2}$ symmetries. (d) f_h of the ground hole state as it varies with the thickness of the spacer. The dot height is 3 nm, and the radius is 8 nm. The highest-energy SQD states and the different regimes of hole localization for the $1S^{+}_{3/2}$ and $1S^{+}_{1/2}$ states are explicitly labeled. The shaded area on the right shows the position of the energy levels in a SQD. The ground state of holes is denoted by solid dots (●) if it is even and by open circles (○) if it is odd.

creases with increasing d. Decreasing the thickness of the spacer in the regime of hole localization labeled by I in Figs. 5(a) and 5(b), a maximum in the energy of the $1S^{\pm}_{3/2}$ and $1S^{\pm}_{1/2}$ states is reached, after which the bonding behavior follows. Then the hole localization enters the II regime, where the confinement of the light holes in the spacer suppresses the confinement of the heavy holes inside the dots. In the III regime of hole localization—i.e., for $d<3$ nm—there exists a near degeneracy of states in doublets, which is mainly a result of the existence of large effective quantum dots for the light holes in the matrix, as manifested in the PD distribution, displayed below. Figure 5 shows that each untwining of the doublets is associated with an anticrossing. States of equal parity strongly anticross near $d=3$ nm. The dependence of the $1S^{\pm}_{3/2}$, $1S^{\pm}_{1/2}$, and $1P^{\pm}_{5/2}$ energy levels is shown in Fig. 5(c) and variation of f_h of the ground hole state with d is shown in Fig. 5(d), respectively. In the SQD the ground hole state has the $S^{+}_{3/2}$ symmetry, but in the TDM's, quantum mechanical coupling between holes and different localizations of the heavy and light holes enables the $1S^{\pm}_{1/2}$ states to be the ground state for $0<d<2.8$ nm and also for 5.7 nm$<d<$15.1 nm. As Figs. 2(e) and 2(f) indicated, the decrease of the hh effective potential energy inside the central dot in the I regime favors the localization of the heavy holes near the radial boundary, and the effective potential well for the light holes is too weak to localize them in the spacers. Due to the mixing of the hole states, the $1P^{+}_{5/2}$ state becomes the ground hole state which occurs near the switching of the hole localization from the spacer to the matrix. This occurs in the narrow range of d from 2.8 to 3.9 nm.

To inspect more closely the binding of holes in the TDM's, we plot in Figs. 6(a)–6(c) the PD of the ground $f_h=3/2$ triplet, composed of the states $1S^{+}_{3/2}$, $1S^{-}_{3/2}$, and $2S^{+}_{3/2}$. The hole clouds in Fig. 6 are shown for $d=1$, 3, 6, 10, and 20 nm, and also the distribution of the hole PD in the $1S^{+}_{3/2}$ SQD state is shown separately at the right of the three panels. For spacers as thin as 1 nm, the hole clouds are localized in the matrix, where the large effective quantum dots for the light holes arise due to strain. As related to the doublet structure and near degeneracy of the states shown in Fig. 5(a), the PD distributions in the $1S^{+}_{3/2}$ and $1S^{-}_{3/2}$ states are similar. Although the confining potential allows the localization of the heavy holes in the central dot, no considerable parts of the heavy holes are found for $d=1$ nm. When the distance between the dots increases to 3 nm, the lh clouds outside the stack fade and relocate to the spacer regions. The $1S^{-}_{3/2}$ and $2S^{-}_{3/2}$ states anticross in the range 3 nm$<d<$6 nm, which leads to an exchange of their spatial localizations. The $2S^{+}_{3/2}$ and $2S^{-}_{3/2}$ and also $3S^{+}_{3/2}$ and $3S^{-}_{3/2}$ levels are twined for $d<9.5$ nm (see Fig. 5). The anticrossings between the levels of equal parity untwine the doublets, which results in a relocation of the holes in the $2S^{+}_{3/2}$ state. When increasing d from 10 to 20 nm, the lh clouds in the $1S^{+}_{3/2}$ and $2S^{+}_{3/2}$ states decrease, which positions the holes mainly inside the dots. Due to the larger confining potential for the heavy holes in the satellite quantum dots [see Figs. 2(b) and 2(e)], the PD's of the $1S^{\pm}_{3/2}$ states for $d=20$ nm are composed of two larger clouds in the satellite dots, while the holes in the $2S^{+}_{3/2}$ state are localized in the central dot.

The reconfiguration due to quantum mechanical coupling and strain is also present in the $S^{\pm}_{1/2}$ hole states in the TDM's, as shown for the $1S^{+}_{1/2}$, $1S^{-}_{1/2}$, and $2S^{+}_{1/2}$ states in Figs. 7(a)–7(c). The PD distributions in the highest-energy states of both parities in the SQD's are shown separately at the right of the three panels. The doublet structure of the first two states is apparent in the leftmost column of Fig. 7. Separating the quantum dots furnishes more space for the light holes in the spacer regions; therefore, they transfer from the matrix to the dots, which additionally gives rise to anticrossings between the hole levels in the range from 2 to 4 nm [see Fig. 5(b)]. As a consequence, the hole wave functions are substantially reconstructed. Even though the extrema of the effective potentials favor heavy holes in case of thick spacers, the value of $F_h=\hbar/2$ does not allow for the hh state to contribute noticeably, and the light holes dominate for $d=10$ nm. When continuing towards $d=20$ nm, the hh clouds emerge in all three states due to anticrossings. For $d=20$ nm, the hole PD's of all three states resemble those of uncoupled quantum dots, which indicates that the reconstruction is almost completed for $d=20$ nm. However, the $2S^{+}_{1/2}$

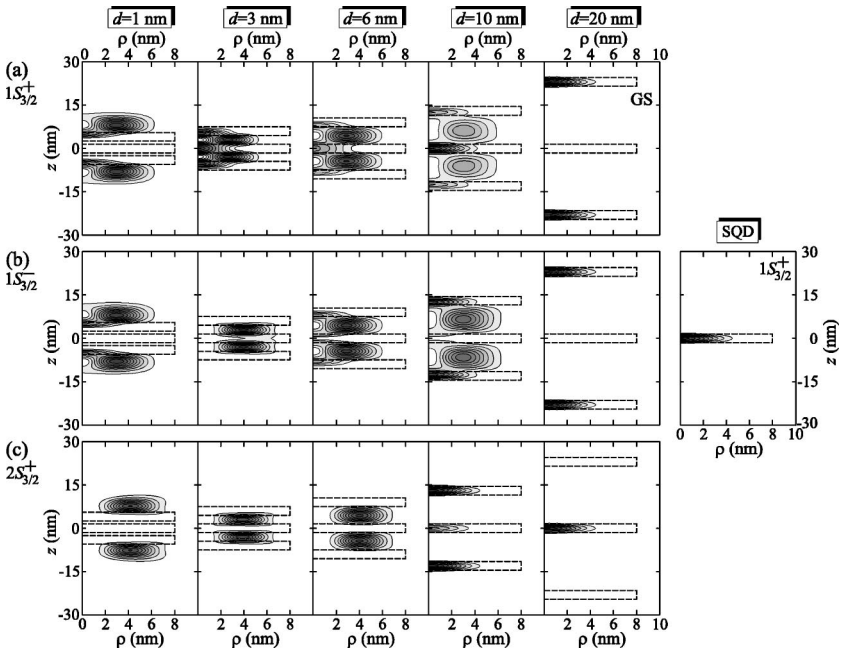

FIG. 6. The PD's of the highest energy $S_{3/2}$ VB triplet in the TDM for $h=3$ nm and $d=1$, 3, 6, 10, and 20 nm: (a) the $1S^+_{3/2}$ state, (b) the $1S^-_{3/2}$ state, and (c) the $2S^+_{3/2}$ state. The PD distribution of holes in the $1S^+_{3/2}$ SQD state is shown to the right of the three panels. GS denotes the ground states, and the dot boundaries are indicated by the dashed lines.

PD distribution appears to be similar to the PD distribution of the $1S^+_{1/2}$ SQD state and is likely to be transferred to the $1S^+_{1/2}$ TDM state for even thicker spacers. The difference between the PD distributions of the $1S^+_{1/2}$ and $1S^-_{1/2}$ states for $d=20$ nm arises from the opposite parity, which effectively removes the hole clouds from the central dot in the $1S^-_{1/2}$ state.

C. Exciton states

Both electron and hole zone-center states exhibit double Kramers degeneracy; therefore, *each exciton energy is fourfold degenerate*. Examples of these quartets are

$$Q_1^+ = \left[\boxed{S^+_{-1\uparrow}}_{(x,y)}\, S^-_{+2\uparrow}\, \boxed{S^-_{+1\downarrow}}_{(x,y)}\, S^+_{-2\downarrow}\right], \quad (17a)$$

$$Q_1^- = [S^-_{-1\uparrow} S^+_{+2\uparrow} S^+_{+1\downarrow} S^-_{-2\downarrow}], \quad (17b)$$

$$Q_2^+ = [S^+_{0\uparrow} S^-_{+1\uparrow} S^+_{-1\downarrow} S^-_{0\downarrow}], \quad (17c)$$

and

$$Q_2^- = \left[\boxed{S^-_{0\uparrow}}_{(z)}\, \boxed{S^+_{+1\uparrow}}_{(x,y)}\, \boxed{S^-_{-1\downarrow}}_{(x,y)}\, \boxed{S^+_{0\downarrow}}_{(z)}\right]. \quad (17d)$$

The superscripts here are chosen according to the ordering of

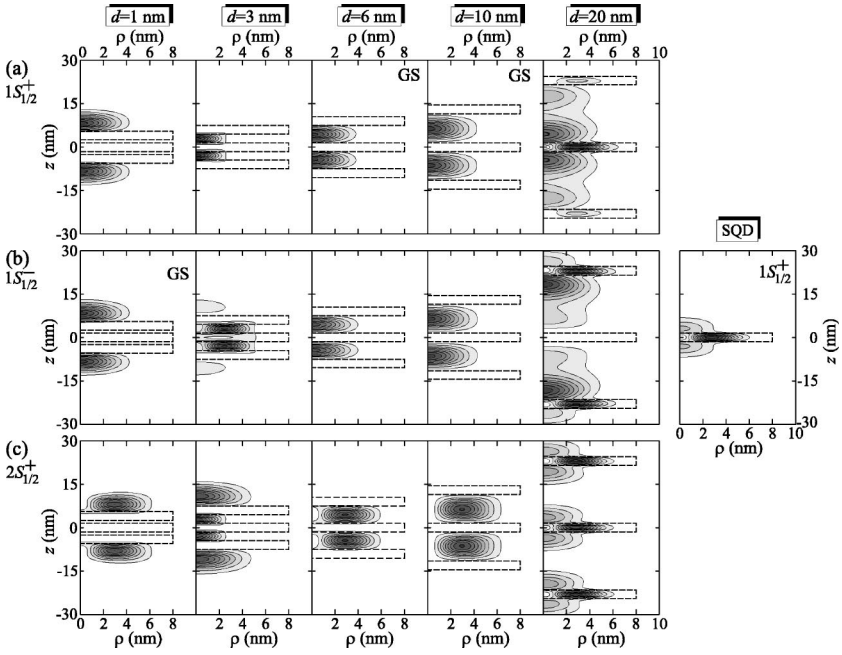

FIG. 7. The PD distribution for the three highest-energy $f_h=1/2$ VB states in the TDM, composed of $h=3$ nm high quantum dots, as function of the spacer thickness, for the same five values of d as in Fig. 6: (a) the $1S^+_{1/2}$ state, (b) the $1S^-_{1/2}$ state, and (c) the $2S^+_{1/2}$ state. The ground state is indicated by GS and the dot boundaries by the dashed lines.

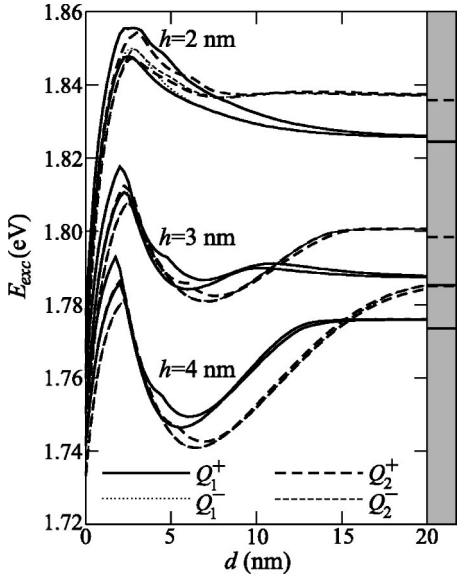

FIG. 8. Variations of the energies of the even-exciton states in TDM's with the spacer thickness. The lowest energy $Q_1^{\pm}$ and $Q_2^{\pm}$ exciton quartets are shown. The solid and thick dashed lines show Q_1^+ and Q_2^+ energy levels, respectively, while the dotted and thin dashed lines display the energies of the Q_1^- and Q_2^- quartets, respectively.

the SQD exciton states; i.e., $1Q_1^+$ and $1Q_2^+$ states have the lowest energies among the four displayed quartets in the SQD. The selection rules for the zone-center periodic parts of the Bloch states allow that only some exciton states in the quartets are optically active, which is indicated by the boxes around the labels of the exciton states and the subscripts which denote the light polarization. For the quartet given in Eq. (17a), for example, the $S^+_{-1\uparrow}$ and $S^-_{+1\downarrow}$ are bright exciton states, while the $S^-_{+2\uparrow}$ and $S^+_{-2\downarrow}$ appear as dark.

The different behavior of electrons and holes with d increases the complexity of the exciton spectra with respect to the analyzed single-particle electronic structures. The electron states adhere to the s^+ symmetry in the ground state, in contrast to the z projection of the angular momentum of the ground hole states which depends on d. These peculiarities are reflected in the exciton energy levels as function of d, as shown in Fig. 8 for the lowest-energy $Q_1^{\pm}$ and $Q_2^{\pm}$ quartets in the 2-, 3-, and 4-nm-high quantum dots, respectively. All exciton energies in the TDM exhibit triplet ordering and overshoots on the SQD exciton energy levels. Larger overshoots, which are shifted towards lower d, are found here than in the electron spectra and consequently cannot be solely attributed to the electrons. The quantum mechanical coupling turns all exciton levels into bonding for thin spacers, and all levels approach the states in the SQD much faster than the hole levels, which may be ascribed to the Coulomb interaction. The SQD energies of the Q_1^+ and Q_2^+ quartets are displayed as the horizontal lines in the gray areas at the right of Fig. 8. The ground exciton state for thick (thin) spacers is provided by the $1Q_1^{\pm}$ ($1Q_2^{\pm}$) quartet and decays for $h=2$ nm and $d \gtrsim 2$ nm, chiefly due to the less pronounced variation of the hole energy levels for large d,[27] while a local minimum is found in the exciton spectra for the other two selected values of the quantum-dot height.

The exciton localization in TDM's is similar to the hole localization as a function of d, as shown by the diagrams of the 2DPD distributions in the optically active $1Q_1^+$ and $1Q_2^-$ exciton quartets in Figs. 9(a) and 9(b), respectively. The 2DPD's of the SQD exciton states are given to the right of the main panels. We find that the extent of the exciton 2DPD is reduced with respect to the PD of holes (see Figs. 6 and 7). Since the electrons are localized inside the quantum dots, the relocation of holes mainly induces the relocation of the exciton wave functions in TDM's when d varies. When d increases from 1 to 3 nm, the exciton clouds shift from the matrix to the spacers and also span the central quantum dot. Further increase of d removes the cloud from the central dot, while those in the satellite dots remain. The evolution of the exciton 2DPD in the $1Q_2^-$ exciton quartet passes through a few phases, with a ring-shaped exciton cloud constrained to the satellite quantum dots emerging for $d=20$ nm.

Due to the largest hh part in the hole states, the SQD exciton states are mainly composed of the heavy holes, as shown in the gray areas in Figs. 10(a) and 10(b), for the $1Q_1^+$ and $1Q_2^+$ SQD quartets, respectively. For thick spacers, the composition of the TDM is also dominated by the heavy holes, as shown in Figs. 10(a) and 10(b) for the optically active $1Q_1^+$ and $1Q_2^-$ states. On the other hand, for low d, the exciton states of both quartets are mainly composed of light holes, while the crossings between different parts take place in the intermediate region. The sharp features in Fig. 10 are

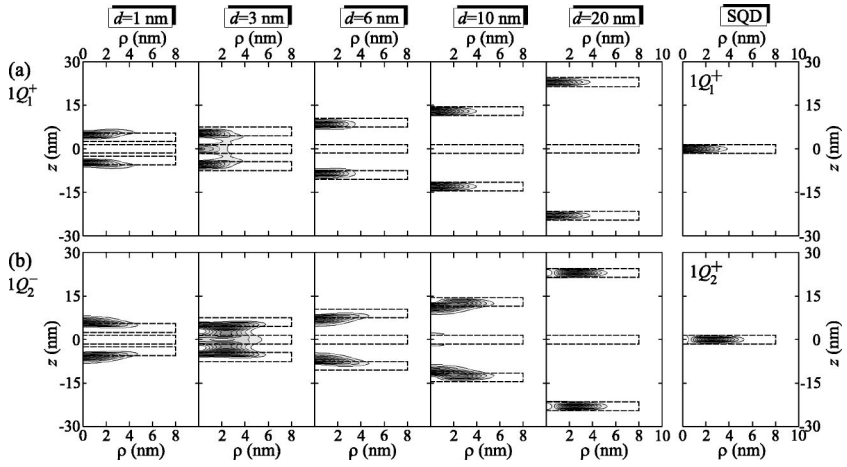

FIG. 9. The spacer-thickness-induced variations in the exciton 2DPD, for (a) the $1Q_1^+$ quartet and (b) the $1Q_2^-$ quartet. Five values of the spacer thickness are selected to show the evolution of the probability density in the TDM composed of 3-nm-high quantum dots. For each state, the distribution of the PD in the SQD is displayed in a separate figure to the right of the main panels. The interfaces between the dots and the matrix are indicated by the dashed lines.

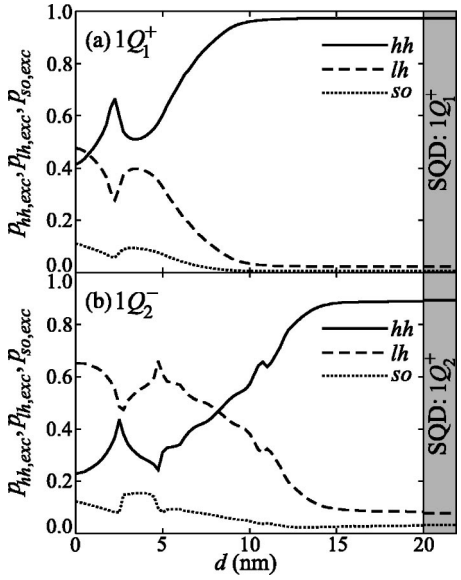

FIG. 10. The dependence of the relative contributions of the different VB's in the ground even-exciton states in the TDM: (a) $1Q_1^+$ and (b) $1Q_2^-$ states. The height (radius) of each quantum dot is 3 nm (8 nm). The hh parts are indicated by the solid lines, and the dashed lines indicate the lh part, while the so parts are shown by the dotted lines. The horizontal lines in the gray areas denote the corresponding SQD values.

produced by anticrossings, and p_{so} is generated by the mixing between the so and lh bands. For $d=0$ this amounts to 11% and 12% of the total probability in the $1Q_1^+$ and $1Q_2^-$ TDM quartets, respectively, while for the exciton states in the SQD they are almost of no relevance. All parts converge well to the values in the single quantum dot as d increases.

D. Comparison with experiment

The SAQD's realized by present growth techniques exhibit a variety of shapes—e.g., pyramids, truncated pyramids, cones, lenses, and disks. The knowledge of shape and size is of paramount importance for a good comparison between theory and experiment. However, the strain present during the growth manifest itself in an increase of the lateral quantum-dot dimensions as subsequent layers are added to the stack, which may lead to a localization of particles mainly in one of the dots in the stack, thereby affecting the symmetry of the electronic structure in quantum-dot molecules. A good control of size and shape in the vertical direction is also spoiled by a possible compositional intermixing between the dot and matrix. Hence, currently fabricated quantum-dot molecules are systems with an asymmetry, and InP/InGaP quantum-dot molecules are no exception, as presented in Ref. 28 and analyzed by magnetophotoluminescence techniques in Ref. 16. The large difference between the experimental and theoretical conditions is especially emphasized for thin quantum dots where a small variation of the dimensions brings about a large modification of the energy spectra.

Despite all differences in the experimental and theoretical conditions, we compared the experimental data with our theoretical results in Fig. 11. The sharp features in the computed curves arise from either anticrossings or angular momentum transitions in the ground state. The experimental photoluminescence energy for $d\to\infty$, shown by the box at the right of Fig. 11 is close to the result for the $h=2$ nm high quantum dot, as indeed found for the height of the analyzed quantum dots, but the energies in the TDM are closer to $h=3$ or 4 nm. The discrepancy between theory and experiment is most probably caused by a poor control of the vertical and lateral dimensions of the quantum dots and the presence of possible compositional intermixing between the dot and matrix. Unfortunately, at present no scanning tunneling microscopy (STM) study of overgrown $InP/In_{0.49}Ga_{0.51}P$ quantum dots and quantum-dot molecules has been made. Furthermore, the measurements were done for only three values of d, which represent an incomplete set of data to preclude a high-quality comparison between theory and experiment and especially to verify the increase of the transition energies above the level in the SQD found by our approach.

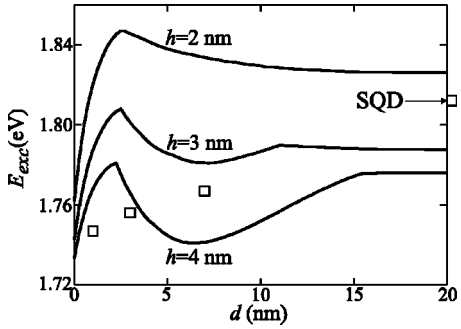

FIG. 11. Variations of the ground exciton energies with d, computed for three values of the quantum-dot height, are compared with the experimental results shown by the boxes. The box at the right of the main figure is the transition energy in the SQD.

Aside from the poor quantitative comparison between experiment and theory for the value of the exciton energy, we may nevertheless state that the experimentally derived conclusions about the hole spatial localization[16] are confirmed by our theoretical analysis. As a matter of fact, the large contribution of the light holes, mainly localized in the spacer for $d\gtrsim 3$ nm, is found in our model. Our theoretical approach provides refinements of both the experimental findings and the single-band model,[26] and gives much deeper insight into the coupling of holes in the strained quantum-dot molecules.

IV. CONCLUSION

We considered the energy levels of electrons, holes, and excitons in self-assembled quantum-dot molecules which consist of three vertically arranged InP/InGaP quantum dots, with staggered type-II band alignment in the unstrained case. The quantum dots have cylindrical shape and are symmetrically arranged in the stacks, which enabled us to introduce the axial approximation for the electronic structure and to classify states according to their parity. The effects of the varying distance between the dots on the electron, hole, and exciton energies and their wave functions were studied. We

found that the strain counteracts quantum mechanical coupling in the conduction band for large distance between the dots, producing antibonding lowest-energy states in the *s*, *p*, and *d* shells. Binding of the holes in quantum-dot molecules is basically established by the light holes located in the spacers. For thin spacers ($d \sim 1$ nm), however, holes settle in the matrix near the bases of the stack. As a consequence, hole states appear as doublets of nearly degenerate states for small *d*. Similar to electrons, the lowest-exciton-energy levels of different angular momenta in quantum-dot molecules exceed the ground-state energy of the single quantum dot, but as a result of the mixing between the valence bands and strain variation with the spacer thickness, both maxima and minima of the hole energies as function of *d* are found. Depending on the height, exciton energies may oscillate with *d*, and they are split by only a few meV. Moreover, the ground exciton states exhibit angular momentum transitions. Our results on the positional localization of the hole and electron confirm qualitatively the magnetophotoluminescence experiments in a pulsed magnetic field of Ref. 16.

ACKNOWLEDGMENTS

This work was supported by the European Commission GROWTH program NANOMAT project, Contract No. G5RD-CT-2001-00545, the University of Antwerp (GOA and VIS), the Belgian Science Policy, and the Serbian Ministry of Science. We would like to acknowledge fruitful discussions with B. Partoens, A. Schliwa, P. Hawrylak, and M. Hayne.

*On leave of absence from Faculty of Electrical Engineering, University of Belgrade, Serbia. Electronic address: milan.tadic@ua.ac.be;tadic@kiklop.etf.bg.ac.yu

†Electronic address: francois.peeters@ua.ac.be

[1] D. Bimberg, M. Grundmann, and N. N. Ledentsov, *Quantum Dot Heterostructures* (Wiley, London, 1999).

[2] L. Jacak, P. Hawrylak, and A. Wójs, *Quantum Dots* (Springer, Berlin, 1998).

[3] Y. M. Manz, A. Christ, O. G. Schmidt, T. Riedl, and A. Hangleiter, Appl. Phys. Lett. **83**, 887 (2003).

[4] D. Bimberg and N. Ledentsov, J. Phys.: Condens. Matter **15**, R1063 (2003).

[5] A. M. Adawi, E. A. Zibik, L. R. Wilson, A. Lemaitre, J. W. Cockburn, M. S. Skolnick, M. Hopkinson, G. Hill, S. L. Liew, and A. G. Cullis, Appl. Phys. Lett. **82**, 3415 (2003).

[6] M. Borgstrom, T. Bryllert, T. Sass, B. Gustafson, L.-E. Wernersson, W. Seifert, and L. Samuelson, Appl. Phys. Lett. **78**, 3232 (2001).

[7] H. Pettersson, L. Bååth, N. Carlsson, W. Seifert, and L. Samuelson, Appl. Phys. Lett. **79**, 78 (2001).

[8] Q. Xie, A. Madhukar, P. Chen, and N. P. Kobayashi, Phys. Rev. Lett. **75**, 2542 (1995).

[9] R. Heitz, A. Kalburge, Q. Xie, M. Grundmann, P. Chen, A. Hoffmann, A. Madhukar, and D. Bimberg, Phys. Rev. B **57**, 9050 (1998).

[10] L. P. Kouwenhoven, D. G. Austing, and S. Tarucha, Rep. Prog. Phys. **64**, 701 (2001).

[11] B. Partoens and F. M. Peeters, Phys. Rev. Lett. **84**, 4433 (2000).

[12] L. R. Fonseca, J. L. Jimenez, and J. P. Leburton, Phys. Rev. B **58**, 9955 (1998).

[13] C. Pryor, Phys. Rev. Lett. **80**, 3579 (1998).

[14] A. Schliwa, O. Stier, R. Heitz, M. Grundmann, and D. Bimberg, Phys. Status Solidi B **224**, 405 (2001).

[15] W. Sheng and J. P. Leburton, Phys. Rev. Lett. **88**, 167401 (2002).

[16] M. Hayne, R. Provoost, M. K. Zundel, Y. M. Manz, K. Eberl, and V. V. Moshchalkov, Phys. Rev. B **62**, 10324 (2000).

[17] J. Persson, M. Holm, C. Pryor, D. Hessman, W. Seifert, L. Samuelson, and M.-E. Pistol, Phys. Rev. B **67**, 035320 (2003).

[18] M. Tadić, F. M. Peeters, and K. L. Janssens, Phys. Rev. B **65**, 165333 (2002).

[19] K. L. Janssens, B. Partoens, and F. M. Peeters, Phys. Rev. B **67**, 235325 (2003).

[20] M. Grundmann, O. Stier, and D. Bimberg, Phys. Rev. B **52**, 11969 (1995).

[21] O. Stier, M. Grundmann, and D. Bimberg, Phys. Rev. B **59**, 5688 (1999).

[22] Al. L. Efros, M. Rosen, M. Kuno, M. Nirmal, D. J. Norris, and M. Bawendi, Phys. Rev. B **54**, 4843 (1996).

[23] F. B. Pedersen and Y.-C. Chang, Phys. Rev. B **53**, 1507 (1996).

[24] C. Pryor, M.-E. Pistol, and L. Samuelson, Phys. Rev. B **56**, 10404 (1997).

[25] M. Tadić, F. M. Peeters, K. L. Janssens, M. Korkusiński, and P. Hawrylak, J. Appl. Phys. **92**, 5819 (2002).

[26] K. L. Janssens, B. Partoens, and F. M. Peeters, Phys. Rev. B **69**, 235320 (2004).

[27] M. Tadić and F. M. Peeters, in *Proceedings of the 26th International Conference on Physics of Semiconductors, Edinburgh*, 2002, edited by A. R. Long and J. H. Davies, Institute of Physics, Conference Series No. 171 (IOP, Bristol, 2003), P208.

[28] M. K. Zundel, P. Specht, K. Eberl, N. Y. Jin-Phillipp, and F. Phillipp, Appl. Phys. Lett. **71**, 2972 (1997).